The Astrophysical Journal, 674:1201–1206, 2008 February 20

A FRESH VIEW OF THE EXTREME-ULTRAVIOLET CORONA FROM THE APPLICATION OF A NEW IMAGE-PROCESSING TECHNIQUE

Guillermo Stenborg
Department of Physics, Catholic University of America, 620 Michigan Avenue, NE,
Washington, DC 20064; stenborg@kreutz.nascom.nasa.gov

and

Angelos Vourlidas and Russell A. Howard
Code 7663, Naval Research Laboratory, Washington, DC 20375;
vourlidas@nrl.navy.mil, russ.howard@nrl.navy.mil
Received 2007 May 15; accepted 2007 November 6

ABSTRACT

The Extreme-ultraviolet Imaging Telescope (EIT) on board the *Solar and Heliospheric Observatory* (*SOHO*) has provided (and continues to provide) the solar physics community with an unprecedented view of the extreme-ultraviolet (EUV) transition region and corona. In particular, it has observed EUV bright points, coronal holes, loops, and arcades, as well as dynamical events such as flares, EIT waves, and mass ejections. However, the multiscale nature of the observed solar features has not been fully exploited so far. In this paper, we introduce a technique to enhance the EUV features based on their multiscale nature, show a few examples of features not revealed with standard image-processing techniques (and therefore not previously noticed in the EIT data set), and make the solar physics community aware of the availability of the full EIT data set as processed with this novel technique.

Subject headings: Sun: activity — Sun: corona — Sun: UV radiation — techniques: image processing

Online material: mpeg animations

1. INTRODUCTION

The observations from the Extreme-ultraviolet Imaging Telescope (EIT; Delaboudiniére et al. 1995) have greatly increased our knowledge of the structure and dynamics of the solar corona over the last 10 yr. The EIT images have revealed the early phases of coronal mass ejections (CMEs; Dere et al. 1997), discovered coronal waves associated with CMEs (Thompson et al. 1998), and detected reconnection at the base of coronal hole plumes (Wang et al. 1998), among other things. It would be natural to assume that the EIT instrument has exhausted its "discovery" potential by now. We will show that this is not the case. We have devised a novel image-cleaning technique and applied it to the EIT database. The strength of the technique lies in its ability to remove the instrumental stray-light background and enhance the fine coronal structures at the same time. The cleaned images reveal such a wealth of structures and dynamics that they appear to have been obtained by a new instrument. The clarity of the enhanced images allows us to identify numerous and potentially interesting phenomena that were previously obscured by stray light and image noise. We have completed the processing of the full EIT mission database to date and have made the movies available online.[1] This paper aims to bring the availability of this resource and its potential for significant discoveries to the attention of the solar physics community. In § 2, we describe the cleaning technique in detail, and in § 3 we present a few of the most interesting observations that we came across during our preliminary inspection of the images. We conclude in § 4.

2. A NOVEL EUV IMAGE-CLEANING TECHNIQUE

Solar images contain complex hierarchical structures. It is common to find structures (e.g., loops) embedded within larger structures (loop arcades), which in turn are within even bigger features (streamers). By looking at different scale sizes, one can identify a myriad of new structures. Moreover, no two solar events are alike, at least from a morphological point of view. In particular, extreme-ultraviolet (EUV) images contain both pseudostatic (relatively stable in the timescale of the EIT cadence of tens of minutes) and dynamic structures that are apparently so rich in small-scale details that they are often misinterpreted or even missed with the use of straightforward image-processing techniques, including standard edge-enhancement techniques.

Basically, the major reasons for poor visualization are (1) the minor difference in the signal strength between the structures and background (especially above the limb) and (2) the multiscale nature of the coronal features. Hence, the visualization of coronal structures and events will always be a challenge for current techniques. Image contrast, for example, is an important tool for disentangling the different structures in a given region. Histogram equalization techniques, in particular, are attractive due to their simplicity and low computational time. However, for solar images with a finite number of gray levels, information loss can occur due to quantization errors. A subtle edge (i.e., a small intensity gradient in a direction perpendicular to the structure at any point) may be merged with its neighboring pixels and thus disappear. Even simple adaptive histogram equalization using a local fixed region in the transformation cannot adapt to features of distinct sizes, which are common in coronal structures. On the other hand, the common strategy for the majority of the classical edge-enhancement algorithms is that of edge detection followed by sharpening. In its simplest form, one can highlight edges by adding the high-frequency components of the image to the original image several times (unsharp masking). The problem with the unsharp-masking-based techniques lies in their single-scale nature; they are not effective for images containing small-scale structures embedded in larger features.

[1] See http://lasco-www.nrl.navy.mil.

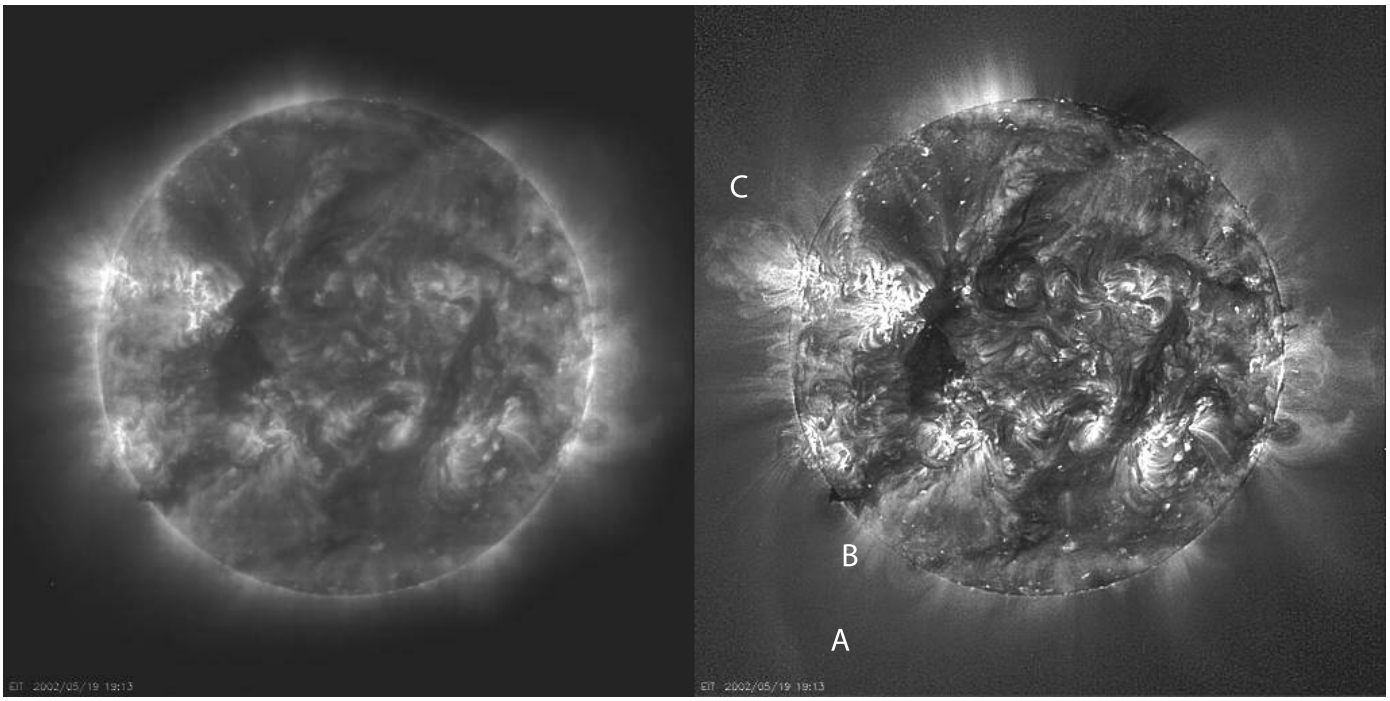

FIG. 1.—Comparison between a regularly processed EIT 195 Å image (*left*) and the same image processed with our wavelet technique (*right*) using the same color scale. The wavelet-processed image looks sharper overall, and several structures such as the cavity (B) and postflare loops (C) are much clearer. Note the long loop (A), which is invisible in the untreated image with this scaling (see corresponding online movie).

In brief, the multiscale nature of coronal features is the reason that standard image-processing methods do not work so efficiently (Stenborg & Cobelli 2003, hereafter Paper I). Multiresolution approaches, i.e., those techniques by which an image can be decomposed into its different components at different scales (spatial frequencies), are the proper next step. The wavelet transform is a popular multiresolution approach because it presents considerable advantages over traditional methods: it is able to discriminate structures as a function of scale and shape, and thus is able to detect, enhance, and filter small-scale structures embedded within larger scale features.

2.1. *Details of the New Cleaning Technique*

Most books address the application of the wavelet transform to signals in the time domain. In that case, a timescale decomposition of the signal is obtained. We are interested in its application to two-dimensional intensity maps. The extrapolation is straightforward if one thinks of the time domain as the spatial extent of the image. Therefore, the wavelet transform applied to a 2D intensity map will result in a 2D space scale decomposition of the image.

The wavelet transform analyzes signals by means of (1) dilation and compression, i.e., scaling, of an analyzing wavelet (therefore, it adapts to frequency) and (2) translations, i.e., shifting, of the analyzing wavelet over the signal domain. The resulting wavelet coefficients are a measure of the correlation between the wavelet and a localized section of the signal. The continuous wavelet transform (CWT) uses discretely sampled data (a continuous signal sampled in discrete picture elements or pixels). The shifting process is a smooth operation across the length of the sampled data, and the scaling can be defined from a minimum (original signal scale) to a maximum chosen by the user, thus giving a much finer resolution. The trade-off for this improved resolution is the increased computational time and memory required to calculate the wavelet coefficients.

In particular, the 2D version of the so-called *a-trous* CWT (Holschneider & Tchamitchian 1990; Shensa 1992) produces a set of resolution-related views of the image, called wavelet scales (or planes), plus a smoothed version of the original image. The sum of all the wavelet scales plus the smoothed version of the image returns the original image (hereafter we will call this process "reconstruction"). Moreover, since the wavelet transform is not its own inverse, each scale can be considered as an image and can be further decomposed (wavelet splitting). In Paper I, we developed a contrast-enhancement technique based on the wavelet-splitting algorithm to enhance the internal structure of CMEs observed by the LASCO coronagraphs on board *SOHO*. In its simplest form, the enhancement algorithm works as a sophisticated unsharp-masking filter, where different weight is given to each wavelet scale before reconstruction. With this approach, the wavelet-enhanced version of a given image is not unique, by which we mean that different enhanced versions of the image can be obtained by choosing different parameters for the algorithm (which weights are assigned to each scale, the shape and size of the kernel used, the direction in which the wavelet transform is performed, etc.). The selection of a given set of parameters will depend on the aim of the study.

In this work, we extend the work initiated in Paper I to enhance the images obtained with the EIT in the four available wavelengths (171, 195, 284, and 304 Å). The EIT images contain remnant instrumental noise and stray light, even after being treated with the standard reduction steps (dark current subtraction, exposure time normalization, degrid, flat field, and degradation corrections). To improve the visibility of the EUV structures, these problems must be taken into account.

Our new algorithm is a two-step procedure that can be customized according to the aim of the study. The first step is designed to increase the relative intensity of the high-frequency components, w_j, of the images via the 2D version of the *a-trous* and weighted recomposition. We used a 2D B3-spline as kernel for

the *a-trous* decomposition. After several kernel sizes were tested, we found the best results with a kernel $3 \times$ CCD plate scale ($7.7''$ for full-resolution EIT images; $15.5''$ for half-resolution images). Unfortunately, the enhancing process works not only on the solar structures but also on instrumental patterns in the images, for example, on any residual grid pattern not properly removed by the calibration routines. To account for this, each wavelet scale used for reconstruction had to be corrected by an appropriate mask, W_j^i. The correction consisted of the subtraction of an empirical model from the corresponding scales. The corresponding models are obtained as the median of the daily median images at each scale over a 4 week period centered on the image under treatment.

The second step is aimed at preserving and highlighting the slowly varying components of the signal by removing the residual scattered light and instrumental noise. To create a model of the scattered light, R^i, for a given frame, we calculated the minimum over a 4 week period of daily median images centered around the frame under treatment. For practical purposes, all the images in a given month were treated with the same model. This approach is similar to that used for the creation of the LASCO C2 and C3 background models (Morrill et al. 2006).

In general terms, for a one-level decomposition scheme, the reconstruction recipe used to enhance the EIT images can be written as

$$I_k^{\text{treated}} = \left[\log(I_k > 0) - \log\left(R^i > 0\right)\right] + \sum \alpha_j \left(w_j - W_j^i\right), \tag{1}$$

where α_j is the weight given to the corresponding scales. The set of α values used on the reconstruction depends on the user needs and the plate scale (i.e., half-resolution images are subject to a slightly different reconstruction scheme compared to the full-resolution images). An example of the visual improvement achieved by this technique is shown in Figure 1. The standard image on the left appears as though viewed through a dirty lens compared to the wavelet-enhanced image on the right (processed in full resolution and reconstructed using $\alpha = [1, 30, 5]$). This is especially obvious for the structures above the limb, which suffer most from stray-light effects.

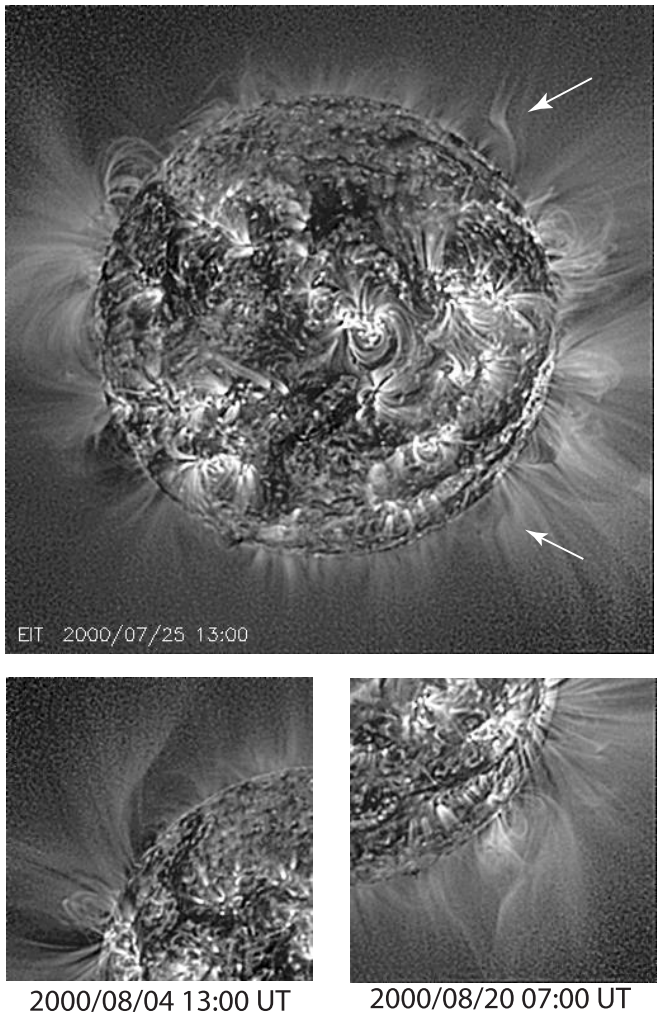

FIG. 2.—EIT 171 Å images processed by our technique (half-resolution, reconstructed using $\alpha = [1, 7, 1]$), showing a wealth of off-limb structure. The arrows point to loop structures that may correspond to null-point locations. The structures remain stable over at least a few rotations, as expected for null points. The two bottom subfields are further examples of coronal null-point candidates and large-scale loops extending beyond 1.4 $R_\odot$.

3. RESULTS AND DISCUSSION

We applied our technique to the full database of the EIT images from 1996 onward. The processed images show a great wealth of fine-scale structures and EUV emission extending to the edge of the EIT field of view. We have selected a couple of examples of processed EIT images to demonstrate the improvements achieved by our technique and its potential for providing new insights into the dynamics of the corona.

3.1. *Identification of Possible Coronal Null Points*

The processing of the 171 Å images reveals a highly structured EUV corona out to at least 1.4 $R_\odot$, the very edge of the EIT field of view (Fig. 2). Since these observations were obtained during solar maximum, the 171 Å emission is dominated by active region scale loops. Rather surprisingly, the processed images reveal many large loops that extend beyond the field of view of the instrument (e.g., Fig. 2, *bottom left*). These loops went largely unnoticed in the standard images. One of the most striking aspects of the enhanced images, however, is the detection of loops with sharp upward bends. Such examples are marked with arrows in Figure 2. A possible interpretation for these unusual structures is that they are EUV manifestations of magnetic null points, locations where the coronal magnetic field goes to zero. According to the theory (e.g., Priest & Forbes 2000), the magnetic configuration around a 3D null point resembles a fan, as field lines emanating from a large number of footpoints meet at the null point and form a spine (a current sheet) that extends upward. If the magnetic field strength at opposite sides of the underlying neutral line varied considerably, it could lead to nonuniform heating at the legs of the loops. In that case, only part of the fan would be bright in the EUV at any given moment, resulting in shapes similar to those seen in Figure 2. This is just a plausibility argument, however. The magnetic field configuration must also provide support for the existence of null points in these locations. To check this, we have used a potential-field source-surface (PFSS) extrapolation to the observed field for this Carrington rotation, CR 1956. The extrapolation shown in Figure 3 was provided by Y.-M. Wang and was calculated from Mount Wilson observations. An extrapolation based on Kitt Peak observations gave very similar results. The figure shows the PFSS model corresponding to the full-disk image in Figure 2 and the model for seven days earlier, when the structure in question was near disk center. A quick inspection of the extrapolations

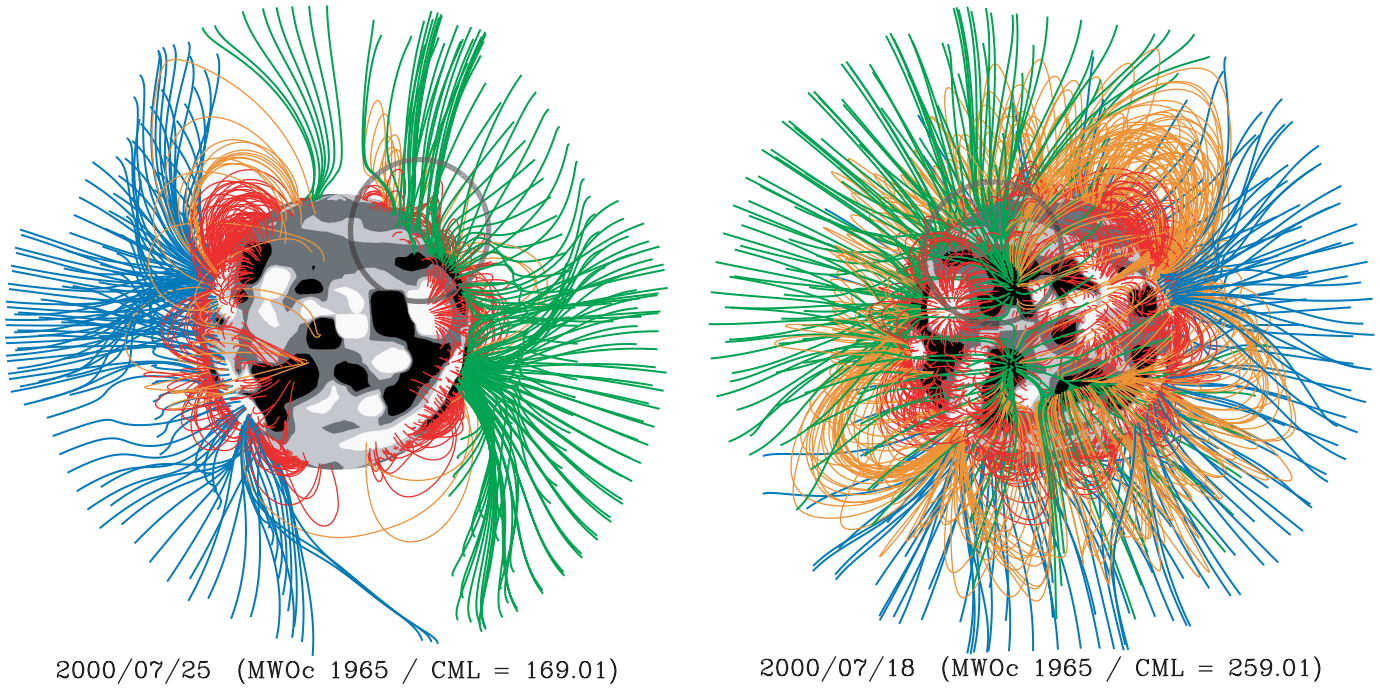

FIG. 3.—PFSS extrapolations of the coronal magnetic field on 2000 July 25 (*left*) and rotated by 90° in longitude (*right*). The extrapolations were based on Mount Wilson photospheric maps for Carrington Rotation 1956. Open field lines are shown in blue (green) if directed outward (inward). Closed field lines above 1.5 $R_\odot$ are shown in orange, or otherwise in red. Black, dark gray, light gray, and white denote ares of the photosphere where $B_r < -10$ *G*, -10 *G* $< B_r < 0$ *G*, 0 *G* $< B_r <$ $+10$ *G*, and $B_r > +10$ *G*, respectively. The circles mark the area corresponding to the null-point candidate in the EIT image. It corresponds to the location of a pseudostreamer.

suggests that the unusual EUV structures are bounded by two coronal holes of the same polarity and overlie two neutral lines. This is precisely the requirement for the creation of a pseudostreamer, which has been shown to be an X-type null point (Wang et al. 2007). This is a strong indication that these EUV structures are indeed coronal null points.

Null points are the subject of intense research because of their importance in energy release during flares and CMEs (Ugarte-Urra et al.2007; Aulanier et al. 2000). However, they are difficult to observe directly. We are unaware of any direct observations of null points at the coronal heights seen in our 171 Å images. The structures in Figure 2 may be the best candidates so far. They are stable structures and last for several rotations, as expected for potential field structures, and their scale heights correspond to potential magnetic field scales. These arguments do not, however, prove that all such upward-bent structures are null points. A more detailed investigation is required, but it is beyond the scope of this paper.

3.2. *Detection of Coronal Condensations and Downflows in the High Corona*

The application of our technique to the 304 Å EIT images has important implications due to the properties of the 304 Å bandpass. The image processing enhances the fine-scale structures in the quiet Sun network and in prominences that originate in the He I line at temperatures around 80,000 K. However, the 304 Å bandpass also contains the Si XI line at 303.4 Å, which arises in coronal temperatures of about 1.8 MK. The Si XI emission is diffuse, and is best seen off-limb over active regions. The removal of the stray light allows us to observe solar structures in both temperature regimes simultaneously. For example, we can see very clearly both the hot coronal cavity and the cool prominence embedded in it over the southwest limb in Figure 4. Interestingly, this system erupted later that day, and the processed images offer insights into the dynamics of the eruption and the interplay between the cavity and the prominence. The analysis of this event is, however, beyond the scope of this paper.

Another intriguing observation in the enhanced 304 Å images is the straightforward detection of coronal condensations and downflows in large-scale coronal loops. In Figure 4 (*right*), we show a sequence of observations over the western limb, taken during a high-cadence (7 minute) 304 Å campaign on 2000 January 8. The full movie can be seen in the online version of this article. The frames show very clear formations of small-scale, cool blobs in a coronal loop. Some of them move slowly across the top of the loop and accelerate downwards along the footpoints. For example, the blobs appearing at 7:53 UT start moving toward the southern footpoint with a speed of about 10 km s^{-1}, but they reach the bottom of the loop with a speed of 90 km s^{-1}, implying an acceleration of $\sim$16.9 m s^{-2}. On the other hand, blobs appearing on the northern side of the loop do not seem to move significantly, but rather they coalesce over a couple of hours in a large Y-shaped location (Fig. 4, 14:07 UT), from which several small-scale downflows originate during the rest of the day. The downflows have speeds ($\sim$70–100 km s^{-1}) and accelerations ($\sim$15–17 m s^{-2}) similar to the southern-directed blobs. Such evolution has been predicted by both theoretical calculations and MHD simulations (Karpen et al. 2005). Downflowing 304 Å blobs have been reported by De Groof et al. (2004, 2005) using much higher cadence (68 s) observations. However, only a small number of blobs were analyzed, and they were visible at lower heights than in our observations. The authors invoked modeling to verify that the 304 Å structures were indeed blobs and not waves. In contrast, the treated 304 Å image sequence, visible in Figure 4 and the associated online movie, shows the nature of the blobs very clearly. Cooling flows have

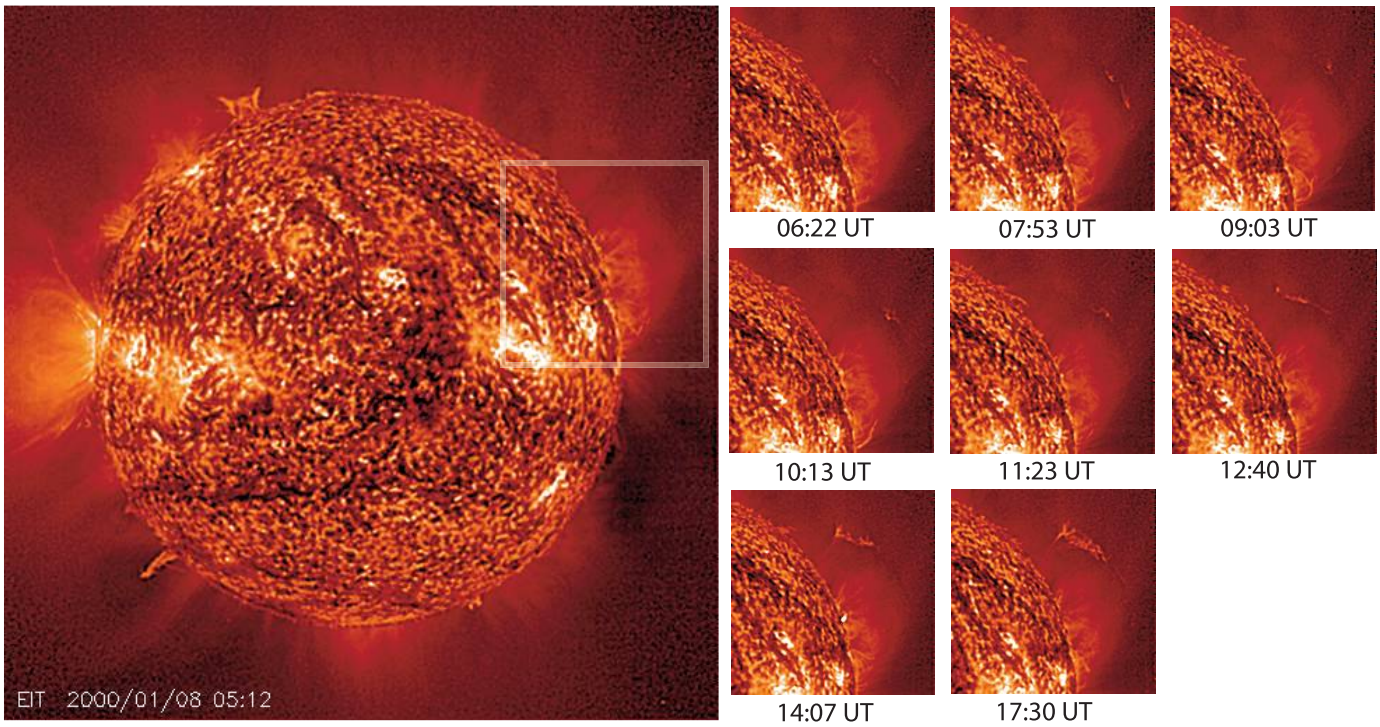

FIG. 4.—EIT 304 Å images processed with our technique (full-resolution, reconstructed using $\alpha = [1, 30, 5]$). The full-disk image clearly shows the two emission components in this passband. The off-limb diffuse loop structures correspond to hot (1.8 MK) emission, while the fine-scale features on the disk and the prominences are cool He I (8×10^4 K). The processed images allow us, for the first time, to study the spatial relationship of the two components simultaneously. The panels on the right zoom in on a structure above the western limb (the field of view is marked by the box in the full-disk image). The time series show an example of coronal condensation in action (see text for details and corresponding online movie).

been indirectly detected in *TRACE* (Schrijver 2001) by following the loop emission from the hotter passbands (195 Å) to the cooler ones (1216 Å).

In summary, our observations confirm the analysis of De Groof et al. (2005) and extend the detection of flows to much higher altitudes. We believe that the EIT observations in Figure 4 are the clearest example yet of coronal condensations high in the corona and show one of the effects specifically predicted by theory, namely, condensation coalescence (Karpen et al. 2005). We plan to analyze this observation in more detail in the near future. It is unclear, at present, how common these events are, since EIT high-cadence observations are rarely taken in the 304 Å wavelength.

4. CONCLUSIONS

Our intent was to present a novel image-processing technique for EUV images and its successful application to the EIT data. The processed images not only have better visual clarity than the standard EIT images, but they also reveal details and structures that went largely unnoticed before. Moreover, the EUV signal can be detected in the cleaned images up to the very far end of the field of view of the instrument. We hope that the two examples presented here are sufficient to demonstrate the scientific potential of the enhanced images. Coronal condensations and magnetic null-point candidates are but a small number of features that become more visible, and thus can be studied more easily in the processed images. We plan to pursue detailed analyses of these structures in future papers. We also note that a similar technique (obviously with a different reconstruction approach) has been applied to the LASCO C2 full data archive. These images, along with those from EIT, are available to everyone as MPEG or (on request) MVI movies from our Web site.[2] We invite the community to download and use these movies for scientific analysis. Currently, we are adapting the technique to the EUV observations from the SECCHI/EUVI full-disk imagers aboard the *STEREO* mission. We hope that processed EUVI images will be available soon.

We thank the referee for useful comments that helped improve the manuscript. We are grateful to Y.-M. Wang for providing the magnetic field extrapolations. This work was supported by NASA funding to the *SOHO* LASCO MO&DA. *SOHO* is an international collaboration between NASA and ESA and is part of the International Solar Terrestrial Physics Program. LASCO was constructed by a consortium of institutions: the Naval Research Laboratory (Washington, DC), the University of Birmingham (Birmingham, UK), the Max-Planck-Institut für Sonnensystemforschung (Katlenburg-Lindau, Germany), and the Laboratoire d'Astronomie Marseille (Marseille, France).

[2] See http://lasco-www.nrl.navy.mil/index.php?p=content/wavelet.

REFERENCES

Aulanier, G., DeLuca, E. E., Antiochos, S. K., McMullen, R. A., & Golub, L. 2000, ApJ, 540, 1126
De Groof, A., et al. 2004, A&A, 415, 1141
———. 2005, A&A, 443, 319
Delaboudiniére, J.-P., et al. 1995, Sol. Phys., 162, 291
Dere, K. P., et al. 1997, Sol. Phys., 175, 601
Holschneider, M., & Tchamitchian, P. 1990, in Les Ondelettes en 1989: Seminaire d'Analyse Harmonique, ed. P. G. Lemarie (Berlin: Springer), 102
Karpen, J. T., Antiochos, S. K., Tanner, S. E. M., & DeVore, C. R. 2005, ApJ, 635, 1319

Morrill, J. S., et al. 2006, Sol. Phys., 233, 331
Priest, E., & Forbes, T. 2000, Magnetic Reconnection (Cambridge: Cambridge Univ. Press)
Schrijver, C. J. 2001, Sol. Phys., 198, 325
Shensa, M. J. 1992, Proc. IEEE, 40, 2464
Stenborg, G., & Cobelli, 2003, A&A, 398, 1185
Thompson, B. J., et al. 1998, Geophys. Res. Lett., 25, 2465
Ugarte-Urra, I., Warren, H. P., & Winebarger, A. R. 2007, ApJ, 662, 1293
Wang, Y.-M., Sheeley, N. R., Jr., & Rich, N. B. 2007, ApJ, 658, 1340
Wang, Y.-M., et al. 1998, ApJ, 508, 899